Chapter 10

Dissociative Chemisorption of Methanol on Cu(111) with Implications for Formaldehyde Formation

This chapter is based on Gerrits, N.; Kroes, G.-J. An AIMD Study of Dissociative Chemisorption of Methanol on Cu(111) with Implications for Formaldehyde Formation. *J. Chem. Phys.* **2019**, *150*, 024706, DOI: 10.1063/1.5070129

Abstract

An important industrial process is methanol steam reforming, which is typically used in conjunction with copper catalysts. However, little agreement exists on the reaction mechanisms involved on a copper catalyst. Therefore, in this chapter research has been performed yielding additional insight into the reaction mechanism for dissociative chemisorption of methanol on Cu(111) using Born-Oppenheimer molecular dynamics, supported by static calculations of the molecule-metal surface interaction with density functional theory. In this chapter, it is predicted that after the initial dissociation, formaldehyde is formed through three different mechanisms. Additionally, it is observed that at high energy, CH cleavage is the dominant pathway instead of the formerly presumed OH cleavage pathway. Finally, in order to describe the interaction of methanol with the metal surface, the SRP32-vdW functional is used, which has been previously developed and tested for CHD_3 on Ni(111), Pt(111), and Pt(211) using the specific reaction parameter (SRP) approach. The SRP32-vdW functional is applied to methanol on Cu(111) as well, in the hope that future experiments can validate the transferability of the SRP32-vdW functional to chemically related molecule-metal surface systems.

10.1 Introduction

Methanol steam reforming is an important industrial process with several applications such as formaldehyde and syngas production. However, there is little agreement concerning the reaction mechanisms of methanol on metal surfaces, especially on copper-based catalysts[1]. Due to the existence of several different chemical bonds, methanol dissociation is described by a complex reaction scheme involving several products that are formed via different pathways. Furthermore, little is known about the mechanisms of the reactions that follow the breaking of the first bond in methanol. For example, experimental evidence for formaldehyde formation on copper catalysts through direct decomposition of methanol exists[2–5], although the underlying pathways remain unclear. So far, theoretical calculations have only been able to deal with this reaction scheme on a static level using transition state theory[6–12], or on a dynamical level but with a frozen surface[13]. However, these levels of theory exclude exchange of energy between the surface atoms and the molecule and transition state theory excludes any dynamical effects such as steering as well. Moreover, although the complete steam reforming reaction of methanol to CO_2 and hydrogen of course also involves water, water only plays a role after the initial reaction steps, i.e., after formaldehyde is formed, by hydrolyzing either a methyl formate intermediate or formaldehyde[1]. Depending on the reaction conditions, the preceding formation of formaldehyde is often the rate controlling step for methanol steam reforming[14–17], and thus an important reaction step to investigate. Therefore, in this chapter water is neglected and only the dissociative chemisorption of methanol and subsequent formation of formaldehyde on Cu(111) is investigated using Born-Oppenheimer molecular dynamics (BOMD) in order to include dynamical effects. Finally, on Pt(111) and Ru(0001) the methanol decomposition mechanism can be affected by the methanol pre-coverage, while no such dependence has been reported on Cu(111), on which methanol has a lower adsorption energy[9]. Since the simulations in this chapter are performed in the zero coverage limit, i.e., only initial sticking of methanol on a clean surface is considered, the results should therefore be relevant for catalysis at sufficiently low pressure and sufficiently high temperatures.

Moreover, to model accurately the interaction between molecules and metal surfaces remains challenging[18–22]. Therefore, the specific reaction parameter (SRP) approach has been used to develop a chemically accurate functional (SRP32-vdW) for methane on Ni(111), Pt(111) and Pt(211)[23, 24]. The SRP32-vdW functional was first developed for CHD_3 + Ni(111)[23]) and later shown to be transferable to methane interacting with metals within the

same periodic table group (CHD_3 + Pt(111)[24]) and with stepped surfaces of that group (CHD_3 + Pt(211)[24, 25]). In this chapter, predictive calculations have been performed on methanol, which is chemically related to methane, and on a metal surface belonging to a neighbouring group of the periodic table. Hopefully, these predictions will be followed by experiments in order to validate the transferability of the SRP32-vdW functional to methanol on a Cu(111) surface.

To summarize, this chapter makes a prediction for the reactivity of methanol on Cu(111), combined with a detailed analysis of the dynamical behaviour. Furthermore, new insights are gained for the reaction mechanisms for the formation of formaldehyde on Cu(111). The chapter is structured as follows: a short summary of the technical details is given in Section 10.2. Moreover, the barriers and elbow plots obtained with static DFT calculations are discussed in Sections 10.3.1 and 10.3.2. In Section 10.3.3 the reaction probabilities are presented, followed by the impact site associated with reactive collisions in Section 10.3.4. Furthermore, Section 10.3.5 concerns the energy transfer of methanol to the surface atoms, and Section 10.3.6 concerns the orientations methanol goes through during the reaction. Finally, formaldehyde formation is discussed in Section 10.3.7, and a short summary is given in Section 10.4.

10.2 Method

The Vienna Ab-initio Simulation Package (VASP version 5.3.5)[26–30] is used for the BOMD and electronic structure (Density Functional Theory, DFT) calculations. A kinetic energy cutoff of 400 eV and a Γ-centered $3 \times 3 \times 1$ k-point grid are used. Moreover, core electrons have been represented with the projector augmented wave (PAW) method[30, 31]. The surface is modeled using a 4 layer (4×3) supercell, where the angle between the u and v vectors is 30° instead of the usual 60°, i.e., a skewed unit cell is used (see also Figure 10.B.1. Furthermore, a vacuum distance of 15 Å is used between the slabs and the top three layers have been relaxed in the Z direction. In order to speed up convergence, first-order Methfessel-Paxton smearing[32] with a width parameter of 0.2 eV has been applied. Convergence of the employed computational setup is confirmed to be within chemical accuracy (1 kcal/mol, or 4.2 kJ/mol) and results connected to this convergence are given in Section 10.A.

Transition states (TSs) are obtained with the dimer method[33–36] as implemented in the VASP Transition State Tools package (VTST)[37], and are confirmed to be first-order saddle points by checking if only one imaginary

frequency is found at the TS. Forces on the degrees of freedom are converged within 5 meV/Å, where the degrees of freedom are for the motion of the methanol atoms.

In order to account for surface temperature effects, the procedure described in Section 2.4.1 is employed. For the BOMD simulations, a surface temperature of 550 K is used, where the atoms in the top three layers are allowed to move in all three directions and the ideal lattice constant is expanded by a factor of 1.0078 in order to reflect the expansion of the bulk due to the surface temperature[38]. Ten differently-initialized slabs are generated using the aforementioned procedure, resulting in a pool of 10 000 snapshots. The average temperature of the ensemble of slabs is (537 ± 54) K.

Methanol molecular beam bundles were simulated according to the parameters in Table 10.1, which were obtained for CHD_3 seeded in H_2 molecular beam bundles in Ref. [23]. It is assumed that methanol has a similar velocity slip in a molecular beam as methane; hence, beam parameters obtained for CHD_3 are used here for methanol. The residual energy E_R (4.2 kJ/mol) is added to the kinetic energy in order to correct for the interaction with the periodic image and to take into account that the interaction of methanol with the surface has not yet decayed to zero, as is described in Sections 2.4.2 and 10.A. The laser-off beams are simulated by sampling the initial vibrational states of the molecule from a Boltzman distribution at nozzle temperature T_n, while the initial angular momentum of the molecules has been set to zero, and the molecules' orientations are randomly sampled. The laser-on beam ($\nu_1 = 1$) is simulated by initializing all molecules with one quantum in the OH stretch mode. Moreover, the experimental R(1) transition to the rotational state $J = 2$ and $K = 0$ is simulated in the BOMD trajectories. It is assumed that the alignment in M of the molecules excited in the experiments[20] is erased by hyperfine coupling due to the long pathway to the surface. Therefore, M has been statistically sampled, i.e., $M = -2, -1, 0, 1, 2$. For the rotational states, the methanol was treated like an oblate symmetric top, in an approximation in which the effect of the hydrogen in the hydroxyl is neglected, taking into account the mass mismatch between the oxygen and hydrogen atoms. The coupling between the internal rotation of the hydroxyl with respect to the methyl, i.e., the torsion vibrational mode, and the rotational states is also neglected in the generation of the initial conditions. Hence, setting up the initial rotational states is done in the same way as for CHD_3 in previous work[23, 24] (see also Section 2.4.2). For every BOMD data point, 500 trajectories were run for up to 1 ps, or until the trajectory was considered to be reacted or scattered, with a time step of 0.4 fs. The rest of the technical details of the BOMD calculations can be found in recent work[23, 24, 39] and in Chapter 2.

TABLE 10.1: Experimental beam parameters that describe the simulated methanol velocity distributions. ν_0 and α are determined through time-of-flight measurements for 600, 750 and 900 K[23]. The parameters for $\langle E_i \rangle = 163.1$ kJ/mol are not from experiment, but theoretical estimates obtained by extrapolation. See the text for further details.

T_n (K)	$\langle E_i \rangle$ kJ/mol	ν_0 (m/s)	α (m/s)
500*	163.1	3177.70	158.89
600	188.7	3418.09	168.02
750	229.2	3760.72	216.91
900	269.5	4070.12	274.51

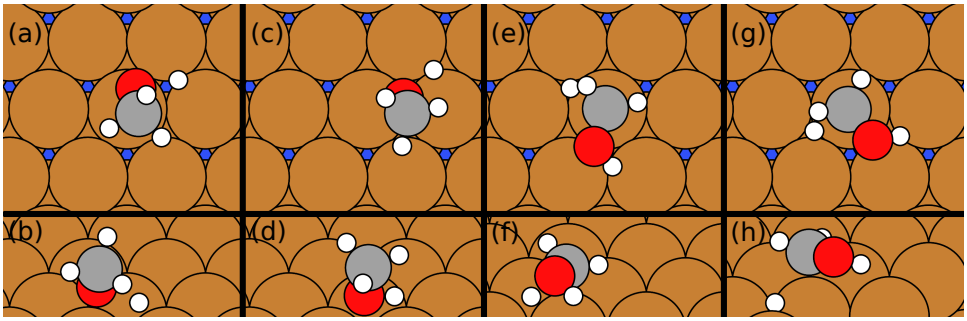

FIGURE 10.1: Top and side view of the TS of methanol on Cu(111) with the OH-fcc1 (a,b), OH-bridge1 (c,d), CH-top1 (e,f), and CH-top2 (g,h) geometries. At the surface, blue circles indicate the fcc sites.

The SRP32-vdW functional previously used for CHD_3 + Ni(111), Pt(111), Pt(211), Cu(111) and Cu(211)[23, 24, 40] is employed here as well, of which the exchange part is defined as

$$E_x = x \cdot E_x^{RPBE} + (1 - x) \cdot E_x^{PBE}, \tag{10.1}$$

where E_x^{RPBE} and E_x^{PBE} are the exchange parts of the RPBE and PBE[41, 42] exchange-correlation functionals, respectively, and $x = 0.32$. Moreover, for the correlation part, the vdW correlation functional of Dion and coworkers (vdW-DF1)[43] is used.

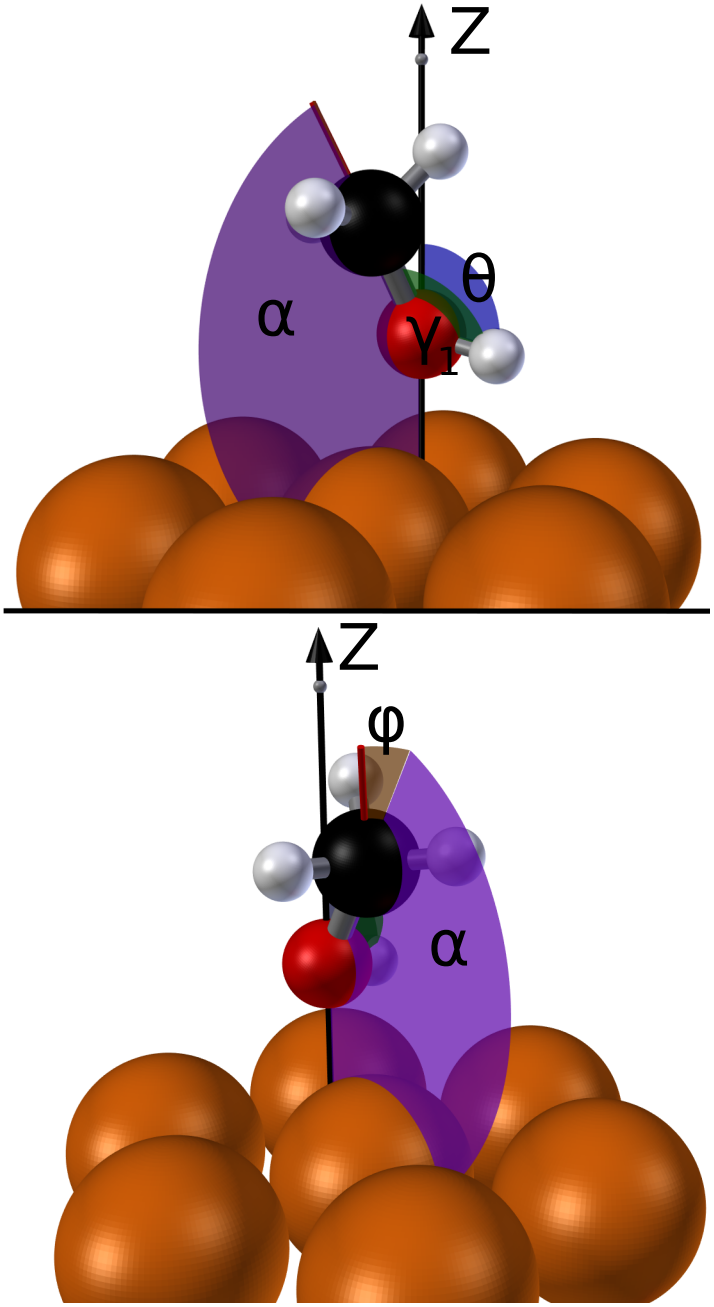

FIGURE 10.2: θ, γ_1, α and ϕ angles used to describe the methanol geometry. See the text for further explanation.

TABLE 10.2: Barrier geometries for methanol on Cu(111). The labels indicate whether OH or CH cleavage occurred and the location of the broken bond. Zero-point energy corrected barriers are given in the brackets.

Label	Z_C (Å)	Z_O (Å)	r (Å)	θ (°)	β (°)	γ_1 (°)	γ_2 (°)	α (°)	ϕ (°)	E_b (kJ/mol)
OH-fcc1	3.06	1.89	1.62	117.8	144.4	64.9	63.9	144.3	1.0	92.4 (75.7)
OH-bridge1	3.11	1.75	1.49	112.5	158.9	59.3	59.6	159.2	0.4	95.1 (78.1)
CH-top1	2.46	2.85	2.03	132.5	110.6	138.0	24.7	73.5	130.3	130.4 (116.2)
CH-top2	2.46	2.87	2.02	134.5	111.8	135.3	24.4	72.5	130.0	130.4 (116.4)

10.3 Results

10.3.1 Barriers

The obtained barrier geometries for methanol on Cu(111) are summarized in Figure 10.1 and Table 10.2. Additionally, the θ, γ_1, α and ϕ angles used to describe the TS geometries in Table 10.2 are depicted in Figure 10.2. θ is the angle between the surface normal and the vector of the dissociating OH or CH bond pointing to the H atom. β denotes the angle between the surface normal and the umbrella axis, which is defined as the vector from the geometric center of the three H-atoms to the carbon atom. Furthermore, γ_1 defines the angle between the vector of the CO bond pointing to the O atom and the dissociating CH or OH bond, whereas γ_2 defines the angle between the umbrella axis and the dissociating CH or OH bond. Finally, α describes the angle between the CO bond and surface normal and ϕ indicates the angle between the umbrella axis and the CO bond.

The lowest barrier height found is for the OH-fcc1 geometry, where the OH bond is broken above the fcc site. The barrier height of this geometry is 92.4 kJ/mol, which is in good agreement with earlier DFT results using the PBE DF[9]. Another barrier for OH cleavage is found above the bridge site (OH-bridge1), which is 2.6 kJ/mol higher than the OH-fcc1 barrier. Both barrier geometries are similar, except for the larger length of the dissociating bond and the larger tilt of the molecule with respect to the surface normal (i.e., β is smaller) of the OH-fcc1 geometry compared to OH-bridge1.

Furthermore, the barrier height found for CH cleavage is considerably higher than OH cleavage (38 kJ/mol higher). The two obtained barriers for CH cleavage have identical barrier heights (130.4 kJ/mol) and similar geometries, where the major difference is the orientation of the molecule with respect to the high-symmetry sites. Moreover, the barrier for CH cleavage is considerably later than for OH cleavage, i.e., the length of the dissociating bond is much larger. From both a dynamical and energetic point of view this would mean that the minimum barrier for OH cleavage is more easily accessible than for CH cleavage. Also, in the barrier geometries for OH cleavage the CO bond is perpendicular to the surface, whereas in the geometries for CH cleavage the CO bond is parallel to the surface. Finally, no barrier is obtained for CO cleavage, but it is expected to be considerably higher than the barriers obtained in this chapter[9].

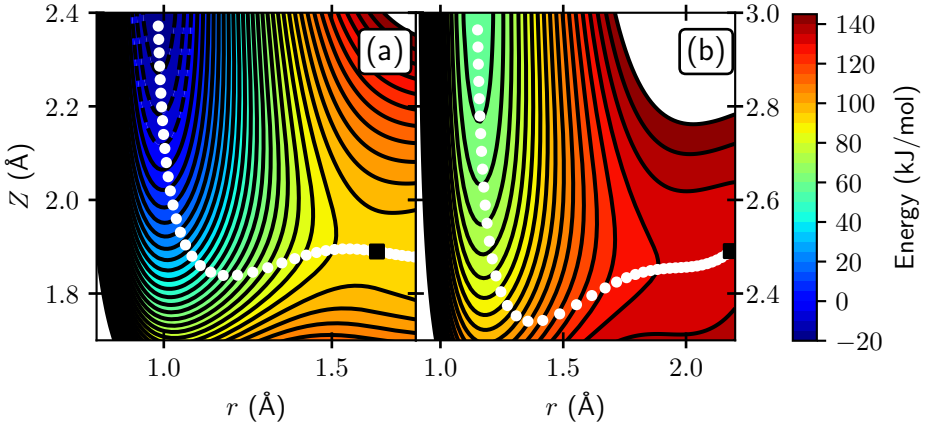

FIGURE 10.3: Elbow plot of methanol on Cu(111), where methanol is fixed in the OH-fcc1 (a) or CH-top1 (b) TS geometry, whereas Z and the length r of the dissociating XH bond (X is C or O) are variable. Contour lines are drawn at intervals of 5 kJ/mol between -20 and 150 kJ/mol. The colours indicate the energy (kJ/mol) with respect to methanol in the gas phase and the black squares indicate the highest point along the MEP (white circles).

10.3.2 Minimum Energy Path

Figure 10.3 shows the elbow plots for the OH-fcc1 and CH-top1 barriers, where methanol is kept fixed in its TS geometry while varying Z and the length r of the dissociating XH bond, where X is O or C. Z is defined as the distance between the surface and oxygen for the OH-fcc1 barrier and between the surface and carbon for the CH-top1 barrier. The OH-fcc1 barrier is earlier (i.e., the length of the dissociating bond is smaller) and closer to the surface than the CH-top1 barrier, as also evident from the aforementioned barrier geometries in Table 10.2. Furthermore, the minimum energy path (MEP) associated with the OH-fcc1 barrier is less curved than the MEP associated with the CH-top1 barrier. This suggests that the OH-fcc1 barrier is not only more accessible than the CH-top1 barrier from a barrier height point of view, but also from a dynamical point of view in connection with the "*bobsled effect*"[44, 45]. Finally, elbow plots have not been obtained for other barrier geometries, however, similar results are expected.

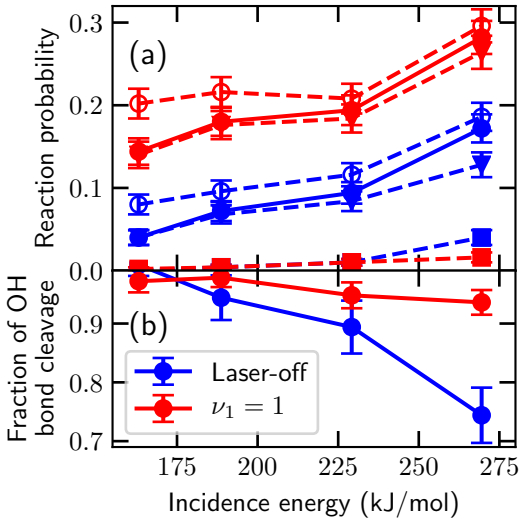

FIGURE 10.4: Reaction probability of methanol on Cu(111) for laser-off (blue) and $\nu_1 = 1$ (red) BOMD simulations (a), and the fraction of reactions that occurred through OH bond cleavage (b). In panel a, squares and triangles indicate dissociation of the CH and OH bond, while the solid circles indicate the total dissociation probability and open circles also include trapping. The error bars represent 68% confidence intervals.

10.3.3 Sticking Probability

A prediction for the reactivity of methanol on Cu(111) using BOMD is presented in Figure 10.4. The vibrational efficacy of exciting the OH stretch mode ($\nu_1 = 1$) is very high compared to the laser-off predictions (about 2). Furthermore, exciting the OH stretch mode suppresses CH cleavage, while for laser-off experiments a higher fraction of CH cleavage is predicted at higher incidence energies. Also, at $\langle E_i \rangle = 270\,\text{kJ/mol}$ about 0.5% of the reacted trajectories were due to CO cleavage, which can be expected due to the very high translational energy of methanol, which exceeds even the high barrier for CO cleavage[9]. Finally, trapping is observed as well, however, due to the timescales involved with trapping it is not possible to obtain statistical data for a reaction probability including a trapping mechanism; i.e., only an upper bound for King and Wells experiments[46] can be given as the sum of the reaction probability and the probability that the molecule is still trapped after 1 ps.

In Figure 10.5, the reaction probabilities computed with the BOMD simulations are shown, where the ground state reaction probabilities are included as well. The ground state reaction probability is obtained from the laser-off simulations by only considering molecules initially in the vibrational ground state. However, for the purpose of obtaining good statistics in the calculation of the ground state reactivity, the torsion vibrational mode (rotation) of the hydroxyl is allowed to be excited since it is excited easily due to its compara-

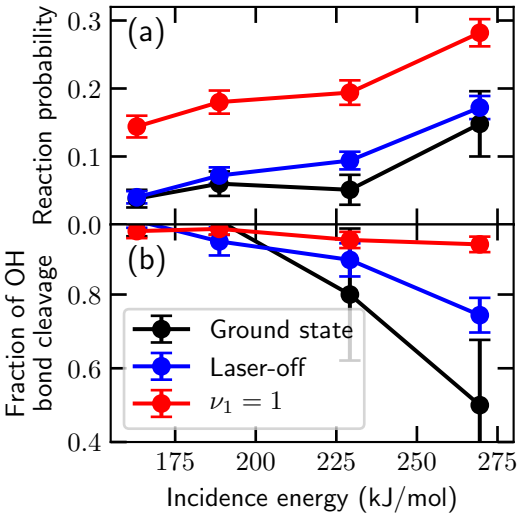

FIGURE 10.5: Reaction probability of methanol on Cu(111) for ground state (black), laser-off (blue) and $\nu_1 = 1$ (red) experimental conditions (i.e., no contribution of trapping is included), as computed with BOMD simulations (a), and the fraction of reactions that occurred through OH bond cleavage (b). The error bars represent 68% confidence intervals.

tively low energy. The ground state reaction probability curve shows similar behaviour as the laser-off curve. However, at high incidence energy, and thus high nozzle temperature, the ground state reaction probability is lower than the laser-off reaction probability due to the higher population of vibrationally excited molecules, with the excited vibrational modes being other modes than the torsion mode, in the molecular beam.

10.3.4 Reaction Site

The distribution of the distance of reacting methanol (only the reaction involving OH cleavage) to the high symmetry sites is given in Figure 10.6 and compared to the statistical distributions. In general, no steering is observed for the methanol in the X and Y directions. Furthermore, as can be seen in Figure 10.7, for the reaction of $\nu = 1$ methanol the distance to the high symmetry sites is statistical. However, at lower incidence energy and under laser-off conditions, methanol is more likely to react closer to the hollow and bridge sites than at the top site. This could mean that methanol does not react over the minimum OH cleavage barrier (OH-fcc1), for which the center of mass of methanol would be above the top site, but rather via the OH-bridge1 barrier above the hollow or bridge site. This may well be as the OH-bridge1 barrier is only 2.6 kJ/mol higher than the OH-fcc1 barrier. Furthermore, the OH-bridge1 barrier is earlier than the OH-fcc1 barrier and thus it should be dynamically more accessible. Finally, due to the small amount of trajectories leading to

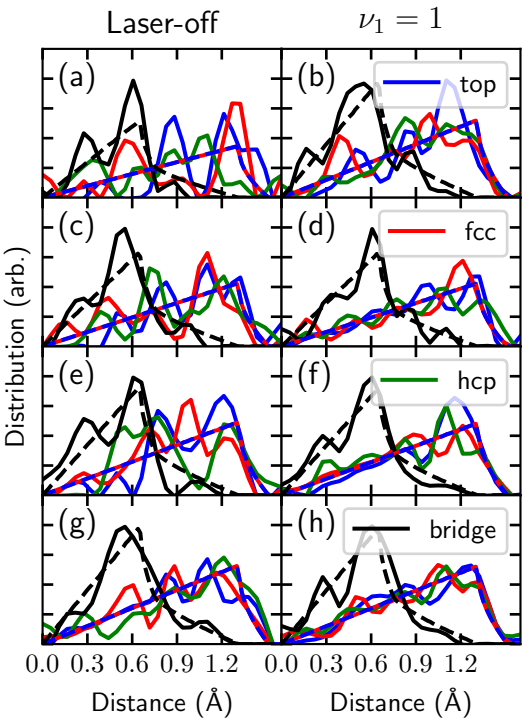

FIGURE 10.6: Distributions of the distance (Å) of the reacting methanol (through OH cleavage) to the closest top (blue), fcc (red), hcp (green) and bridge (black) sites on Cu(111) for laser-off conditions (a,c,e,g) and for $\nu_1 = 1$ (b,d,f,h), with $\langle E_i \rangle = 163$ (a,b), $\langle E_i \rangle = 189$ (c,d), $\langle E_i \rangle = 229$ (e,f) and $\langle E_i \rangle = 270$ kJ/mol (g,h). The blue and red dashed line indicates the statistical distribution for the hollow and top sites, while the black dashed line is the statistical distribution for the bridge site.

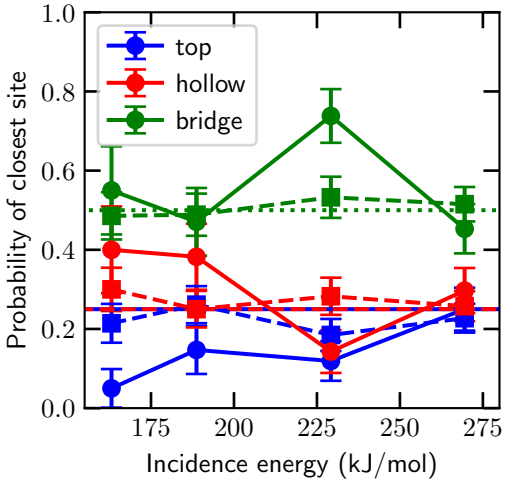

FIGURE 10.7: The probability that a reacting methanol molecule impacts closest to a high-symmetry site is shown for the top (blue), bridge (green), and hollow (red) sites for laser-off conditions (solid lines with circles) and for $\nu_1 = 1$ (dashed lines with squares), as a function of the incidence energy. The dotted green line indicates the statistical average for the bridge site, whereas the red and blue line indicates the statistical average for the hollow and top sites. The error bars represent 68% confidence intervals.

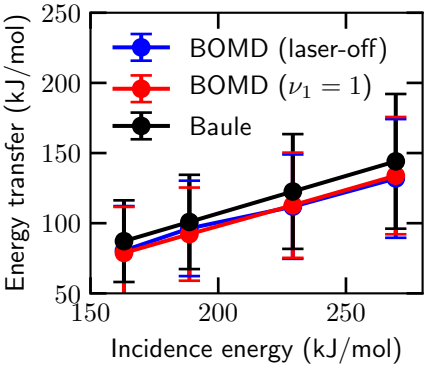

FIGURE 10.8: Energy transfer from scattered methanol to the surface atoms for laser-off conditions (blue) and for $\nu_1 = 1$ (red) as computed from BOMD simulations and the refined Baule model (black)[47, 48], as a function of incidence energy. The error bars represent 68% confidence intervals.

CH or CO cleavage, no conclusions can be drawn regarding the differences between the site specificity for CH and CO cleavage. However, it does seem that at lower energies CH cleavage happens more closely to the top site, which again can be expected from the minimum barrier.

10.3.5 Energy Transfer to the Surface

The average energies transferred by the scattering methanol to the surface atoms predicted by BOMD and by the refined Baule model[47, 48] are compared in Figure 10.8. The formula for the refined Baule model is $E_T = \langle E_i \rangle 2.4\mu/(1+\mu)^2$ (see Section 2.5), where $\mu = m/M$ (with m being the mass of the projectile and M the mass of a surface atom) and $\langle E_i \rangle$ is the average incidence energy. Here, it can be seen that the refined Baule model is in remarkably good agreement with BOMD. Half of the translational energy is transferred to the surface, which is due to the small mass difference between a Cu surface atom and the methanol molecule. Due to this large energy transfer of methanol to the surface, it is expected that surface atom motion plays a considerable role in the reactivity of methanol on Cu(111).

10.3.6 Angular Distributions

Angular distributions of methanol extracted from the BOMD simulations are shown in Figure 10.9. As also noted in the discussion of Figure 10.2, θ indicates the orientation of the dissociating bond, whereas β and α indicate the orientation of the umbrella axis and the CO bond, respectively. Furthermore, ϕ concerns the angle between the CO bond and the umbrella axis, and γ_1 and γ_2 are the angles of the CO bond and umbrella axis with respect to the

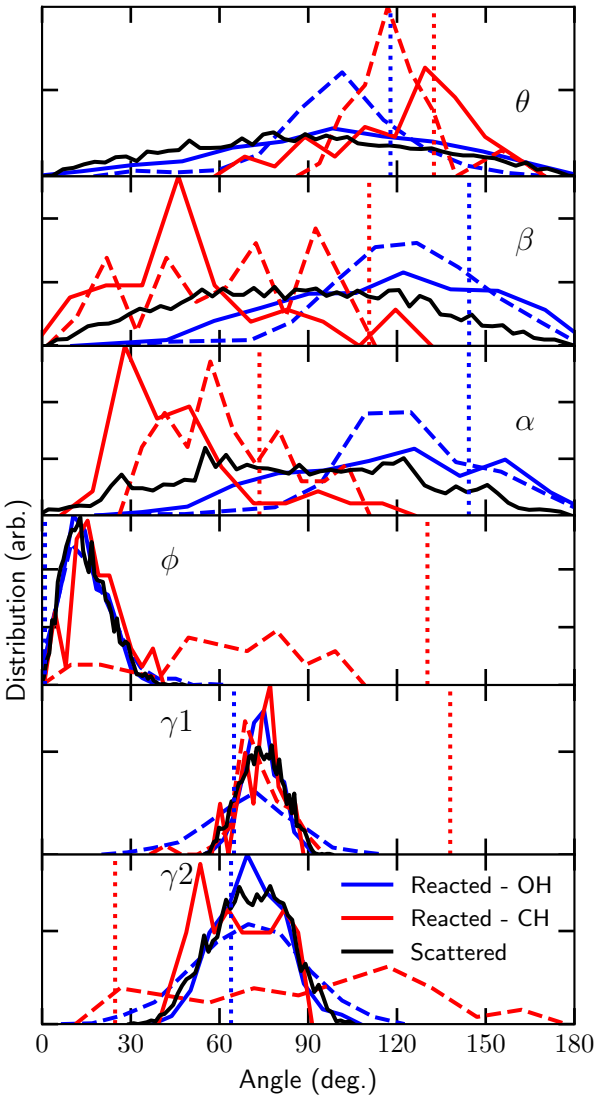

FIGURE 10.9: Angular distributions describing the orientation of methanol during BOMD for scattered (black) and reacted trajectories at the initial time step (solid lines) and when the length of the dissociating bond reaches the TS value (dashed lines). Results for all incidence energies, and simulations of laser-off conditions and for $\nu = 1$ are combined. The blue lines indicate OH cleavage, while the red lines indicate CH cleavage. The vertical dotted lines represent the TS values for the OH-fcc1 (blue) and CH-top1 (red) geometries (see Table 10.2).

dissociating bond. For the initial values, i.e., at $t = 0$ fs, no differences were found between scattered and reacted trajectories in the distributions of the ϕ and γ angles. However, for the θ, β and α distributions differences are found not only between scattered and reacted trajectories, but also between OH and CH cleavage. These differences can be explained by the differences between the TS geometries, since the reacted trajectories tend to have orientations similar to the TS geometries. Exceptions are found for the β, ϕ and γ angles for CH cleavage, where the initial angles cannot be close to the TS geometries since a rather large bend between the umbrella axis and the CO bond is required. Furthermore, for OH cleavage, steering in the θ, β and α angles is observed during the reaction. This means that effectively the orientation of the OH bond relative to the rest of the molecule changes, while the geometry of the rest of the molecule does not change. For CH cleavage considerably more steering is observed than for OH cleavage, with steering in all angles but γ_1 and γ_2. In general, the initial angular distributions for OH cleavage are comparable to the initial angular distributions of the scattered trajectories, whereas this is not the case for the angular distribution for CH cleavage. It seems that dynamically the barrier for OH cleavage is more accessible than the barrier for CH cleavage, which is not only caused by the barrier height and the length of the dissociating bond, but also by the large bend between the umbrella and the CO bond that is required for CH cleavage. Finally, the angle of the CO bond with respect to the surface normal is the most important angle for determining whether OH or CH cleavage will occur.

10.3.7 Formation of Formaldehyde

All reacted trajectories have been propagated for an additional 200 fs after a bond was broken. Some of these trajectories show formation of formaldehyde, for which the probability is provided in Figure 10.10. Formaldehyde is considered to be formed when both a CH bond and an OH bond is broken according to the definition in Section 2.5. Here we see that increasing the incidence energy leads to increased formaldehyde formation. This is probably caused by more energy remaining in the chemisorbed methanol or the hot hydrogen atom after breaking the first bond, which results in a higher chance of breaking the second bond. Furthermore, if the CH bond is broken first, more formaldehyde formation is observed than when the OH bond is broken first. Thus, the increase of CH cleavage with $\langle E_i \rangle$ between 229 and 270 kJ/mol in the laser-off prediction results in a sharp increase of formaldehyde formation, while this is not observed for $\nu_1 = 1$, for which initial CH cleavage is suppressed. Interestingly, previously it was expected that the dominant pathway

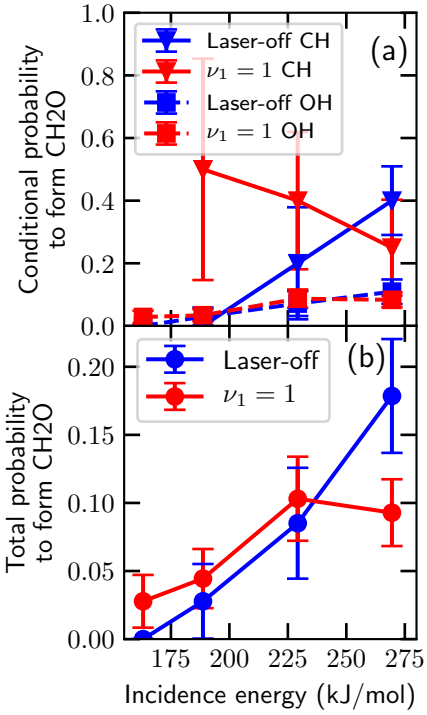

FIGURE 10.10: Probability to form formaldehyde within 200 fs after the first bond is broken for laser-off conditions (blue) and for $\nu_1 = 1$ (green) as computed with BOMD simulations, as a function of incidence energy. Panel a shows the conditional probability to form formaldehyde for when either the CH (solid lines) or the OH bond (dashed) is broken first, while panel b shows the total probability. The error bars represent 68% confidence intervals.

would be via breaking the OH bond first[9], whereas here the opposite result is obtained for high incidence energy. At low energies "OH cleavage first" is the dominant pathway, while at high energies "CH cleavage first" becomes the dominant pathway. Moreover, increasing the $\langle E_i \rangle$ from 229 to 270 kJ/mol with $\nu_1 = 1$ does not increase formaldehyde formation; instead about 1% recombinative desorption of methanol is observed at $\langle E_\mathrm{i} \rangle = 270$ kJ/mol. Also, the conditional probability for laser-off conditions at the highest incidence energy is about 10% as well, suggesting that the conditional probability limit to form formaldehyde after breaking first the OH bond is about 10%.

Three mechanisms for formaldehyde formation have been observed. The first mechanism involves a hot hydrogen atom traveling along the surface, and abstracting another hydrogen atom from the dissociated methanol resulting in formaldehyde and molecular hydrogen, after which both desorb from the surface. The second mechanism also involves a hot hydrogen atom traveling along the surface, but kinetic energy is transferred from the hot hydrogen atom to the dissociated methanol once the hydrogen atom gets close. This results then in formaldehyde and two atomic hydrogens. An accurate evaluation of

the relevance of both mechanisms is hampered by the supercell size, where effectively the hot hydrogen atom interacts with a periodic image. However, this may not be a large issue if we would consider this example to represent a methanol coverage of $1/12^{\text{th}}$ of a monolayer. The third mechanism does not suffer from this periodicity problem, since it involves two bonds to break simultaneously or subsequently, which again results in formaldehyde and atomic hydrogen. Furthermore, only two trajectories resulted in a product where two CH bonds were broken, with no clear relation to the incidence energy or vibrational excitation. Moreover, in one of the two trajectories recombination occurred to CH_2OH. Although these theoretical predictions are for a low methanol coverage, experimental evidence exists for formaldehyde forming from methanol at high pressure, and thus a high methanol coverage, as well[49, 50]. Finally, independent of mechanism in our BOMD calculations, formaldehyde is observed to desorb rapidly after formation due to the relatively low barrier for desorption, which is also observed experimentally[50–52].

10.4 Conclusions

Predictions for the reactivity of methanol on Cu(111) are made using BOMD, supported with an analysis of barriers and elbow plots. It is shown that Cu(111) is highly selective in breaking the OH bond due to the difference in barrier heights and dynamical features of the MEPs for OH and CH cleavage. Moreover, the vibrational efficacy of the OH stretch mode for dissociative chemisorption of methanol is high and vibrationally exciting this mode promotes OH cleavage but suppresses CH cleavage. Furthermore, additional insight is gained into the reaction mechanism following dissociative chemisorption of methanol by propagating reacted trajectories further. Within a short timescale (200 fs) formaldehyde formation is observed for a fraction of the dissociated methanol molecules, for which experimental evidence exists. Three different mechanisms for this formaldehyde production are identified, where two mechanisms involve a hot hydrogen atom that either abstracts another hydrogen atom forming molecular hydrogen or knocks off another hydrogen atom resulting in two hydrogen atoms (i.e., atomic hydrogen is formed) at the surface. In the third mechanism, the OH and CH bonds are broken simultaneously or subsequently without the influence of a hot hydrogen atom. In general, the probability of formaldehyde production is higher at higher incidence energy, and in this case usually a CH bond is broken first. Hopefully, these theoretical predictions will be followed by experiments in order to test

our predictions, which would also provide information on the transferability of the SRP32-vdW functional among similar systems. However, the difference between the surface's work function and molecule's electron affinity is 5.5 eV, and thus it is possible that a GGA DF is unable to correctly describe the barrier height of methanol + Cu(111) (see Chapter 5).

Appendix

10.A Electronic Structure Calculations

Convergence tests have been performed to ensure that the computational setup produces accurate results for the interaction of methanol with Cu(111). To test the convergence, calculations of the minimum reaction barrier height of methanol on Cu(111), i.e., on the barrier for the OH-fcc1 geometry, have been performed. However, the same convergence behavior is expected for other TS geometries. The barrier energy is defined as $E_\mathrm{b} = \epsilon_\mathrm{b} - \epsilon_\mathrm{asym}$, where ϵ_b and ϵ_asym are the energies from the DFT calculations for the barrier geometry and the asymptotic configuration, respectively. The asymptotic configuration is considered to be the gas phase configuration and is obtained by putting the molecule halfway between two periodic slabs, i.e., the distance between the center of mass of methanol and the surface as well as its periodic image is 7.5 Å. The results of the convergence tests are presented in Figure 10.A.1 and Table 10.A.1. The converged setup yields a barrier height of 91.1 kJ/mol, which the employed computational setup (93.7 kJ/mol) can reproduce within chemical accuracy (4.2 kJ/mol). Note that these convergence tests have been performed with single-point calculations (i.e., no TS search was performed), with the TS geometry being obtained with a computational setup employing a (3×3) 5 layer supercell and a $6 \times 6 \times 1$ k-point grid. If a TS search is performed with the computational setup employed throughout this chapter, a barrier height of 92.4 kJ/mol is obtained, i.e., the barrier height is lowered by 1.3 kJ/mol.

The effect of the vacuum distance has also been investigated. When a vacuum distance of 30 Å is employed, while keeping $Z = 7.5$ Å, the interaction energy correction is about 4.2 kJ/mol, where the interaction energy correction is defined as $E_\mathrm{R} = E_\mathrm{b}^{15\,\text{Å}} - E_{\mathrm{b},Z=7.5\,\text{Å}}^{30\,\text{Å}}$. In order to keep the calculations tractable, a vacuum distance of 15 Å is kept, but 4.2 kJ/mol is added to the initial kinetic energy during the BOMD simulations (see Section 2.4.2). This should compensate for the interaction energy correction as at large distance to the surface the interaction energy is only dependent on molecule-surface distance Z, which is shown in figure 10.A.2. In this figure, methanol is kept fixed in its gas phase equilibrium geometry, while varying Z above the top site for a vacuum

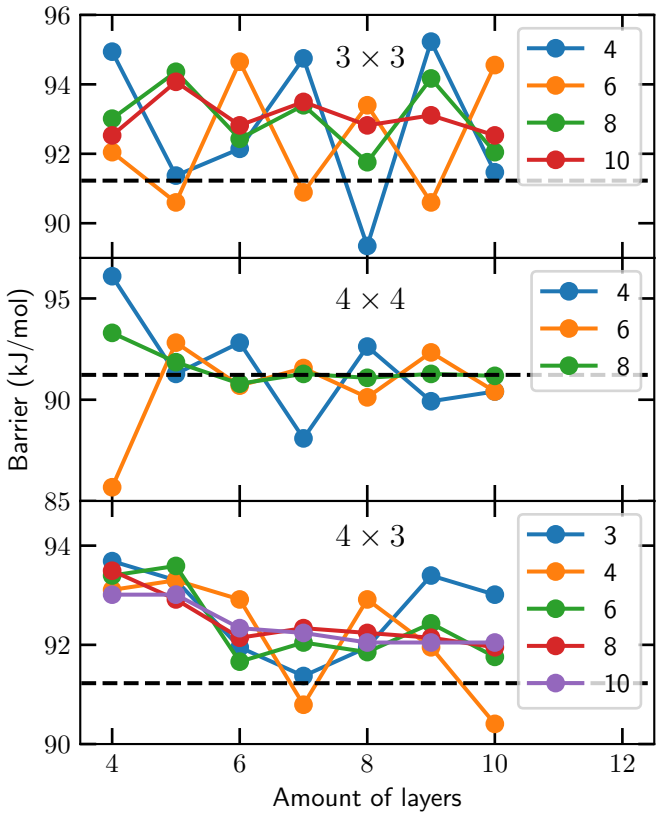

FIGURE 10.A.1: The minimum barrier height for OH cleavage (OH-fcc1 geometry) as a function of the amount of layers for the number of k-points equal to $(n \times n \times 1)$, where n is indicated in the legend. An energy cutoff of 400 eV is used. The first panel is for a 3×3 supercell, the second panel is for a 4×4 supercell, and the last panel is for a 4×3 supercell with a skewed unit cell vector. The dashed lines indicate the converged barrier height and the gray area indicates chemical accuracy (4.2 kJ/mol) with respect to the converged barrier height.

TABLE 10.A.1: The minimum barrier height (kJ/mol) for OH cleavage (OH-fcc1 geometry, see Figures 10.1a,b and Table 10.2) as obtained with specific numbers for the amount of layers and *k*-points, with an energy cutoff of 400 eV. A 3×3, a 4×4 supercell, or a 4×3 supercell with a skewed unit cell vector is employed. The used computational setup is in bold and the most converged result (i.e., obtained with the largest setup) is in italic.

Layers	*k*-points	$E_b, 3 \times 3$	$E_b, 4 \times 3$	$E_b, 4 \times 4$
4	$3 \times 3 \times 1$		**93.7**	
4	$4 \times 4 \times 1$	94.9	93.1	96.1
4	$6 \times 6 \times 1$	92.0	93.4	85.7
4	$8 \times 8 \times 1$	93.0	93.4	93.3
4	$10 \times 10 \times 1$	92.6	93.0	
5	$3 \times 3 \times 1$		93.3	
5	$4 \times 4 \times 1$	91.4	93.3	91.3
5	$6 \times 6 \times 1$	90.6	93.6	92.8
5	$8 \times 8 \times 1$	94.4	92.9	91.9
5	$10 \times 10 \times 1$	94.0	93.0	
6	$3 \times 3 \times 1$		91.9	
6	$4 \times 4 \times 1$	92.1	92.9	92.8
6	$6 \times 6 \times 1$	94.7	91.6	90.7
6	$8 \times 8 \times 1$	92.5	92.1	90.8
6	$10 \times 10 \times 1$	92.8	92.3	
7	$3 \times 3 \times 1$		91.4	
7	$4 \times 4 \times 1$	94.8	90.8	88.1
7	$6 \times 6 \times 1$	90.9	92.1	91.6
7	$8 \times 8 \times 1$	93.4	92.3	91.3
7	$10 \times 10 \times 1$	93.5	92.3	
8	$3 \times 3 \times 1$		91.9	
8	$4 \times 4 \times 1$	89.4	93.0	92.6
8	$6 \times 6 \times 1$	93.4	91.9	90.1
8	$8 \times 8 \times 1$	91.7	92.2	91.1
8	$10 \times 10 \times 1$	92.8	92.1	
9	$3 \times 3 \times 1$		93.4	
9	$4 \times 4 \times 1$	95.2	91.9	90.0
9	$6 \times 6 \times 1$	90.6	92.5	92.3
9	$8 \times 8 \times 1$	94.1	92.2	91.2
9	$10 \times 10 \times 1$	93.1	92.0	
10	$3 \times 3 \times 1$		93.0	
10	$4 \times 4 \times 1$	91.4	90.4	90.4
10	$6 \times 6 \times 1$	94.6	91.8	90.4
10	$8 \times 8 \times 1$	92.1	92.0	*91.1*
10	$10 \times 10 \times 1$	92.5	92.0	

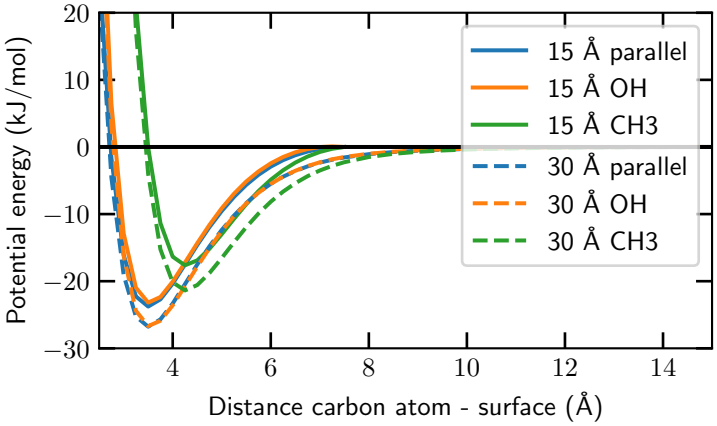

FIGURE 10.A.2: The Van der Waals interaction of methanol with a Cu(111) surface as a function of the distance Z between the surface and the carbon atom, with either the hydroxyl (orange) or methyl (green) group pointing towards the surface, or with the CO bond parallel to the surface (blue). The solid and open lines indicate results obtained with a vacuum distance of 15 and 30 Å, respectively. The asymptotic energy is considered to be zero.

distance of 15 and 30 Å. The Van der Waals well depth is considerably smaller if the methyl group is pointing towards the surface (17.6 kJ/mol) than if the hydroxyl group is pointing towards the surface (23.2 kJ/mol). Moreover, if the CO bond is parallel to the surface the Van der Waals well depth is 0.7 kJ/mol larger than if the hydroxyl group points towards the surface.

Bulk calculations are performed within the primitive unit cell for a fcc lattice, yielding an equilibrium lattice constant $a_0 = 3.679$ Å, which is 1.8% larger than the experimental value $a_0 = 3.615$ Å[53]. The obtained lattice constant was used to model the Cu(111) slab.

10.B Impact Site

The distribution of the impact site of reacting methanol molecules on Cu(111) is provided in Figure 10.B.1 for different incidence energies and for laser-off and $\nu_1 = 1$ conditions.

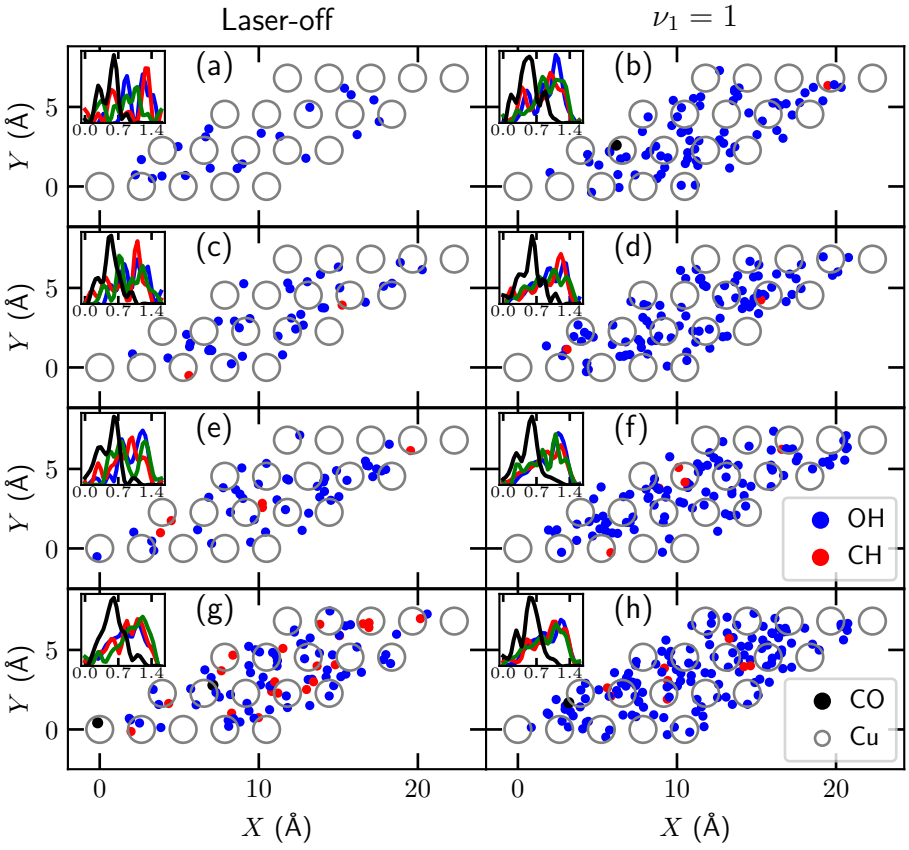

FIGURE 10.B.1: The impact site of reacting methanol on Cu(111) for laser off conditions (a,c,e,g) and for $\nu_1 = 1$ (b,d,f,h), with $\langle E_i \rangle = 163$ (a,b), $\langle E_i \rangle = 189$ (c,d), $\langle E_i \rangle = 229$ (e,f) and $\langle E_i \rangle = 270$ kJ/mol (g,h). The grey open circles indicate the Cu top layer surface atoms, while the small solid circles indicate where dissociation of an OH (blue), CH (red) or CO (black) bond occurred, i.e., when $r = r^{\ddagger}$. The distributions of distance (Å) of the reacting methanol to the closest top (blue), fcc (red), hcp (green) and bridge (black) sites are given in the inset.

References

(1) Sá, S.; Silva, H.; Brandão, L.; Sousa, J. M.; Mendes, A. Catalysts for Methanol Steam Reforming—A Review. *Appl. Catal. B* **2010**, *99*, 43–57, DOI: 10.1016/j.apcatb.2010.06.015.

(2) Russell, J. N.; Gates, S. M.; Yates, J. T. Reaction of Methanol with Cu(111) and Cu(111) + O(Ads). *Surf. Sci.* **1985**, *163*, 516–540, DOI: 10.1016/0039-6028(85)91077-5.

(3) Chen, A.; Masel, R. Direct Conversion of Methanol to Formaldehyde in the Absence of Oxygen on Cu(210). *Surf. Sci.* **1995**, *343*, 17–23, DOI: 10.1016/0039-6028(95)00649-4.

(4) Bowker, M. Active Sites in Methanol Oxidation on Cu(110) Determined by STM and Molecular Beam Measurements. *Top. Catal.* **1996**, *3*, 461–468, DOI: 10.1007/BF02113868.

(5) Wang, Z.-T.; Xu, Y.; El-Soda, M.; Lucci, F. R.; Madix, R. J.; Friend, C. M.; Sykes, E. C. H. Surface Structure Dependence of the Dry Dehydrogenation of Alcohols on Cu(111) and Cu(110). *J. Phys. Chem. C* **2017**, *121*, 12800–12806, DOI: 10.1021/acs.jpcc.7b02957.

(6) Mei, D.; Xu, L.; Henkelman, G. Potential Energy Surface of Methanol Decomposition on Cu(110). *J. Phys. Chem. C* **2009**, *113*, 4522–4537, DOI: 10.1021/jp808211q.

(7) Gu, X.-K.; Li, W.-X. First-Principles Study on the Origin of the Different Selectivities for Methanol Steam Reforming on Cu(111) and Pd(111). *J. Phys. Chem. C* **2010**, *114*, 21539–21547, DOI: 10.1021/jp107678d.

(8) Zuo, Z.-J.; Wang, L.; Han, P.-D.; Huang, W. Insights into the Reaction Mechanisms of Methanol Decomposition, Methanol Oxidation and Steam Reforming of Methanol on Cu(111): A Density Functional Theory Study. *Int. J. Hydrog. Energy* **2014**, *39*, 1664–1679, DOI: 10.1016/j.ijhydene.2013.11.048.

(9) García-Muelas, R.; Li, Q.; López, N. Density Functional Theory Comparison of Methanol Decomposition and Reverse Reactions on Metal Surfaces. *ACS Catal.* **2015**, *5*, 1027–1036, DOI: 10.1021/cs501698w.

(10) Jiang, Z.; Wang, B.; Fang, T. A Theoretical Study on the Complete Dehydrogenation of Methanol on Pd (100) Surface. *Appl. Surf. Sci.* **2016**, *364*, 613–619, DOI: 10.1016/j.apsusc.2015.12.204.

(11) Wang, S.-S.; Gu, X.-K.; Su, H.-Y.; Li, W.-X. First-Principles and Microkinetic Simulation Studies of the Structure Sensitivity of Cu Catalyst for Methanol Steam Reforming. *J. Phys. Chem. C* **2018**, *122*, 10811–10819, DOI: 10.1021/acs.jpcc.8b00085.

(12) Chen, W.; Cubuk, E. D.; Montemore, M. M.; Reece, C.; Madix, R. J.; Friend, C. M.; Kaxiras, E. A Comparative Ab Initio Study of Anhydrous Dehydrogenation of Linear-Chain Alcohols on Cu(110). *J. Phys. Chem. C* **2018**, *122*, 7806–7815, DOI: 10.1021/acs.jpcc.8b01698.

(13) Chen, J.; Zhou, X.; Zhang, Y.; Jiang, B. Vibrational Control of Selective Bond Cleavage in Dissociative Chemisorption of Methanol on Cu(111). *Nat. Commun.* **2018**, *9*, 4039, DOI: 10.1038/s41467-018-06478-6.

(14) Peppley, B. A.; Amphlett, J. C.; Kearns, L. M.; Mann, R. F. Methanol–Steam Reforming on $Cu/ZnO/Al_2O_3$ Catalysts. Part 2. A Comprehensive Kinetic Model. *Appl. Catal. A* **1999**, *179*, 31–49, DOI: 10.1016/S0926-860X(98)00299-3.

(15) Choi, Y.; Stenger, H. G. Fuel Cell Grade Hydrogen from Methanol on a Commercial $Cu/ZnO/Al_2O_3$ Catalyst. *Appl. Catal. B* **2002**, *38*, 259–269, DOI: 10.1016/S0926-3373(02)00054-1.

(16) Lee, J. K.; Ko, J. B.; Kim, D. H. Methanol Steam Reforming over $Cu/ZnO/Al_2O_3$ Catalyst: Kinetics and Effectiveness Factor. *Appl. Catal. A* **2004**, *278*, 25–35, DOI: 10.1016/j.apcata.2004.09.022.

(17) Patel, S.; Pant, K. K. Experimental Study and Mechanistic Kinetic Modeling for Selective Production of Hydrogen via Catalytic Steam Reforming of Methanol. *Chem. Eng. Sci.* **2007**, *62*, 5425–5435, DOI: 10.1016/j.ces.2007.01.044.

(18) Kroes, G.-J. Towards Chemically Accurate Simulation of Molecule–Surface Reactions. *Phys. Chem. Chem. Phys.* **2012**, *14*, 14966–14981, DOI: 10.1039/C2CP42471A.

(19) Jackson, B.; Nattino, F.; Kroes, G.-J. Dissociative Chemisorption of Methane on Metal Surfaces: Tests of Dynamical Assumptions Using Quantum Models and Ab Initio Molecular Dynamics. *J. Chem. Phys.* **2014**, *141*, 054102, DOI: 10.1063/1.4891327.

(20) Wellendorff, J.; Silbaugh, T. L.; Garcia-Pintos, D.; Nørskov, J. K.; Bligaard, T.; Studt, F.; Campbell, C. T. A Benchmark Database for Adsorption Bond Energies to Transition Metal Surfaces and Comparison to Selected DFT Functionals. *Surf. Sci.* **2015**, *640*, 36–44, DOI: 10.1016/j.susc.2015.03.023.

(21) Gautier, S.; Steinmann, S. N.; Michel, C.; Fleurat-Lessard, P.; Sautet, P. Molecular Adsorption at Pt(111). How Accurate Are DFT Functionals? *Phys. Chem. Chem. Phys.* **2015**, *17*, 28921–28930, DOI: 10.1039/C5CP04534G.

(22) Kroes, G.-J. Toward a Database of Chemically Accurate Barrier Heights for Reactions of Molecules with Metal Surfaces. *J. Phys. Chem. Lett.* **2015**, *6*, 4106–4114, DOI: 10.1021/acs.jpclett.5b01344.

(23) Nattino, F.; Migliorini, D.; Kroes, G.-J.; Dombrowski, E.; High, E. A.; Killelea, D. R.; Utz, A. L. Chemically Accurate Simulation of a Polyatomic Molecule-Metal Surface Reaction. *J. Phys. Chem. Lett.* **2016**, *7*, 2402–2406, DOI: 10.1021/acs.jpclett.6b01022.

(24) Migliorini, D.; Chadwick, H.; Nattino, F.; Gutiérrez-González, A.; Dombrowski, E.; High, E. A.; Guo, H.; Utz, A. L.; Jackson, B.; Beck, R. D.; Kroes, G.-J. Surface Reaction Barriometry: Methane Dissociation on Flat and Stepped Transition-Metal Surfaces. *J. Phys. Chem. Lett.* **2017**, *8*, 4177–4182, DOI: 10.1021/acs.jpclett.7b01905.

(25) Chadwick, H.; Gutiérrez-González, A.; Migliorini, D.; Beck, R. D.; Kroes, G.-J. Incident Angle Dependence of CHD_3 Dissociation on the Stepped Pt(211) Surface. *J. Phys. Chem. C* **2018**, *122*, 19652–19660, DOI: 10.1021/acs.jpcc.8b05887.

(26) Kresse, G.; Hafner, J. Ab Initio Molecular-Dynamics Simulation of the Liquid-Metal–Amorphous-Semiconductor Transition in Germanium. *Phys. Rev. B* **1994**, *49*, 14251–14269, DOI: 10.1103/PhysRevB.49.14251.

(27) Kresse, G.; Hafner, J. Ab Initio Molecular Dynamics for Liquid Metals. *Phys. Rev. B* **1993**, *47*, 558–561, DOI: 10.1103/PhysRevB.47.558.

(28) Kresse, G.; Furthmüller, J. Efficient Iterative Schemes for Ab Initio Total-Energy Calculations Using a Plane-Wave Basis Set. *Phys. Rev. B* **1996**, *54*, 11169–11186, DOI: 10.1103/PhysRevB.54.11169.

(29) Kresse, G.; Furthmüller, J. Efficiency of Ab-Initio Total Energy Calculations for Metals and Semiconductors Using a Plane-Wave Basis Set. *Comput. Mater. Sci.* **1996**, *6*, 15–50, DOI: 10.1016/0927-0256(96)00008-0.

(30) Kresse, G.; Joubert, D. From Ultrasoft Pseudopotentials to the Projector Augmented-Wave Method. *Phys. Rev. B* **1999**, *59*, 1758–1775, DOI: 10.1103/PhysRevB.59.1758.

(31) Blöchl, P. E. Projector Augmented-Wave Method. *Phys. Rev. B* **1994**, *50*, 17953–17979, DOI: 10.1103/PhysRevB.50.17953.

(32) Methfessel, M.; Paxton, A. T. High-Precision Sampling for Brillouin-Zone Integration in Metals. *Phys. Rev. B* **1989**, *40*, 3616–3621, DOI: 10.1103/PhysRevB.40.3616.

(33) Henkelman, G.; Jónsson, H. A Dimer Method for Finding Saddle Points on High Dimensional Potential Surfaces Using Only First Derivatives. *J. Chem. Phys.* **1999**, *111*, 7010–7022, DOI: 10.1063/1.480097.

(34) Heyden, A.; Bell, A. T.; Keil, F. J. Efficient Methods for Finding Transition States in Chemical Reactions: Comparison of Improved Dimer Method and Partitioned Rational Function Optimization Method. *J. Chem. Phys.* **2005**, *123*, 224101, DOI: 10.1063/1.2104507.

(35) Kästner, J.; Sherwood, P. Superlinearly Converging Dimer Method for Transition State Search. *J. Chem. Phys.* **2008**, *128*, 014106, DOI: 10.1063/1.2815812.

(36) Xiao, P.; Sheppard, D.; Rogal, J.; Henkelman, G. Solid-State Dimer Method for Calculating Solid-Solid Phase Transitions. *J. Chem. Phys.* **2014**, *140*, 174104, DOI: 10.1063/1.4873437.

(37) Transition State Tools Package for VASP https://theory.cm.utexas.edu/vtsttools/index.html (accessed 02/08/2021).

(38) Mondal, A.; Wijzenbroek, M.; Bonfanti, M.; Díaz, C.; Kroes, G.-J. Thermal Lattice Expansion Effect on Reactive Scattering of H_2 from Cu(111) at T_s = 925 K. *J. Phys. Chem. A* **2013**, *117*, 8770–8781, DOI: 10.1021/jp4042183.

(39) Nattino, F.; Ueta, H.; Chadwick, H.; van Reijzen, M. E.; Beck, R. D.; Jackson, B.; van Hemert, M. C.; Kroes, G.-J. Ab Initio Molecular Dynamics Calculations versus Quantum-State-Resolved Experiments on CHD_3 + Pt(111): New Insights into a Prototypical Gas–Surface Reaction. *J. Phys. Chem. Lett.* **2014**, *5*, 1294–1299, DOI: 10.1021/jz500233n.

(40) Gerrits, N.; Migliorini, D.; Kroes, G.-J. Dissociation of CHD_3 on Cu(111), Cu(211), and Single Atom Alloys of Cu(111). *J. Chem. Phys.* **2018**, *149*, 224701, DOI: 10.1063/1.5053990.

(41) Hammer, B.; Hansen, L. B.; Nørskov, J. K. Improved Adsorption Energetics within Density-Functional Theory Using Revised Perdew-Burke-Ernzerhof Functionals. *Phys. Rev. B* **1999**, *59*, 7413–7421, DOI: 10.1103/PhysRevB.59.7413.

(42) Perdew, J. P.; Burke, K.; Ernzerhof, M. Generalized Gradient Approximation Made Simple. *Phys. Rev. Lett.* **1996**, *77*, 3865–3868, DOI: 10.1103/PhysRevLett.77.3865.

(43) Dion, M.; Rydberg, H.; Schröder, E.; Langreth, D. C.; Lundqvist, B. I. Van Der Waals Density Functional for General Geometries. *Phys. Rev. Lett.* **2004**, *92*, 246401, DOI: 10.1103/PhysRevLett.92.246401.

(44) Marcus, R. A. On the Analytical Mechanics of Chemical Reactions. Quantum Mechanics of Linear Collisions. *J. Chem. Phys.* **1966**, *45*, 4493–4499, DOI: 10.1063/1.1727528.

(45) McCullough, E. A.; Wyatt, R. E. Quantum Dynamics of the Collinear (H, H_2) Reaction. *J. Chem. Phys.* **1969**, *51*, 1253–1254, DOI: 10.1063/1.1672133.

(46) King, D. A.; Wells, M. G. Reaction Mechanism in Chemisorption Kinetics: Nitrogen on the {100} Plane of Tungsten. *Proc. R. Soc. Lond. A* **1974**, *339*, 245–269, DOI: 10.1098/rspa.1974.0120.

(47) Baule, B. Theoretische Behandlung Der Erscheinungen in Verdünnten Gasen. *Ann. Phys.* **1914**, *349*, 145–176, DOI: 10.1002/andp.19143490908.

(48) Goodman, F. O.; Wachman, H. Y. *Formula for Thermal Accommodation Coefficient*; 66-1; Cambridge, Massachusetts: M.I.T. Fluid Dynamics Research, 1966, DOI: 10.21236/ad0631007.

(49) Takezawa, N.; Iwasa, N. Steam Reforming and Dehydrogenation of Methanol: Difference in the Catalytic Functions of Copper and Group VIII Metals. *Catal. Today* **1997**, *36*, 45–56, DOI: 10.1016/S0920-5861(96)00195-2.

(50) Shishido, T.; Yamamoto, Y.; Morioka, H.; Takehira, K. Production of Hydrogen from Methanol over Cu/ZnO and Cu/ZnO/Al_2O_3 Catalysts Prepared by Homogeneous Precipitation: Steam Reforming and Oxidative Steam Reforming. *J. Mol. Catal. A: Chem.* **2007**, *268*, 185–194, DOI: 10.1016/j.molcata.2006.12.018.

(51) Barnes, C.; Pudney, P.; Guo, Q.; Bowker, M. Molecular-Beam Studies of Methanol Partial Oxidation on Cu(110). *J. Chem. Soc., Faraday Trans.* **1990**, *86*, 2693–2699, DOI: 10.1039/FT9908602693.

(52) Greeley, J.; Mavrikakis, M. Methanol Decomposition on Cu(111): A DFT Study. *J. Catal.* **2002**, *208*, 291–300, DOI: 10.1006/jcat.2002.3586.

(53) Mishin, Y.; Mehl, M. J.; Papaconstantopoulos, D. A.; Voter, A. F.; Kress, J. D. Structural Stability and Lattice Defects in Copper: Ab Initio, Tight-Binding, and Embedded-Atom Calculations. *Phys. Rev. B* **2001**, *63*, 224106, DOI: 10.1103/PhysRevB.63.224106.